Journal of Porous Materials (2019) 26:109–119
https://doi.org/10.1007/s10934-018-0624-1

Design of three-dimensional macroporous reduced graphene oxide–Fe_3O_4 nanocomposites for the removal of Cr(VI) from wastewater

Yurong Liu[1] · Zongqiang Zhang[1] · Xiangwei Sun[1] · Tianyu Wang[2]

Published online: 22 May 2018

Abstract
Three-dimensional macroporous reduced graphene oxide–Fe_3O_4 nanocomposites (3D macroporous rGO–Fe_3O_4 nanocomposites) were synthesized through electrostatic self-assembly method. The morphology and structure characteristics of 3D macroporous rGO–Fe_3O_4 nanocomposites were studied in detail. Then 3D macroporous rGO–Fe_3O_4 nanocomposites were used as adsorbents for the removal of Cr(VI) from wastewater. The effects of contact time and solution pH on the adsorption properties of 3D macroporous rGO–Fe_3O_4 nanocomposites were also investigated. Due to the hierarchical porous structure, high surface area and large pore volume, 3D macroporous rGO–Fe_3O_4 nanocomposite adsorbents exhibited excellent adsorption capability and rapid adsorption rates for Cr(VI) from aqueous solution. The kinetic and isothermal studies suggested that the adsorption process could be best described by pseudo-second-order kinetic model and Langmuir isotherm model, respectively. Moreover, the adsorbents could be separated easily by an external magnetic field for reusability, demonstrating great potential for the treatment of wastewater containing Cr(VI) during practical applications.

Keywords Three-dimensional macroporous nanocomposites · Hierarchical porous structure · Reduced graphene oxide · Electrostatic self-assembly · Removal of Cr(VI)

1 Introduction

Heavy metals such as Cr, Hg, Cd, and Pb discharged into environment have high toxicity and bioaccumulation, which has become a serious problem relating to ecological environment and human health [1–5]. Among these heavy metals, Cr(VI) is one of the most harmful pollutant due to its extensive applications in chemical industry, leather tanning, textile manufacturing, steel fabrication, electroplating, nuclear power plant and many other fields [6–9]. Moreover, Cr(VI) is soluble, carcinogenic and accumulated in human body through food chain, causing great damage to human and other living organisms. Therefore, the removal of Cr(VI) from wastewater before being discharged into environment is very significant and urgent.

Recently, many methods including chemical reduction, ion exchange, electrochemical precipitation, membrane separation and bioremediation have been developed to treat Cr(VI)-containing wastewater [10–14]. Most of these methods are effective but requiring a large quantity of chemicals and/or high energy. However, adsorption is an effective and economic method for wastewater treatment because of its many advantages including simplicity, high efficiency, ease of operation as well as the availability of a wide range of adsorbents in comparison with other conventional methods [15].

Graphene has attracted a tremendous amount of attention in recent years because of its perfect sp^2 hybrid carbon nanostructure and high specific surface area [16–19], indicating its potential for the removal of contaminates from wastewater [20–31]. However, it is well-known that two-dimensional lamellar structure of graphene is easily distorted and aggregated into other uncontrolled morphologies because of its

✉ Yurong Liu
liuyr1978@163.com

✉ Tianyu Wang
wangty2@cnooc.com.cn

[1] College of Materials and Chemical Engineering,Research Institute for New Materials Technology, Chongqing University of Arts and Sciences, Chongqing 402160, China

[2] Huizhou Petrochemical Company Limited of China National Offshore Oil Corporation, Guangdong 516081, China

high specific surface area, resulting in a sharp decline in performance [32]. Therefore, it is of great significance to develop an efficient and facile strategy to transform two-dimensional graphene nanosheets into three-dimensional graphene networks with controlled morphology and porous structures [33]. On the other hand, it is difficult to separate graphene from aqueous solution even by high-speed centrifugation because of its small particle size [34–36]. Therefore, developing magnetic graphene-based adsorbents which combine the advantages of high adsorption capacity and separation convenience will be beneficial for the removal of toxic pollutants from wastewater [37–39].

However, to the best of our knowledge, there are still few works about the synthesis of three-dimensional magnetic graphene-based nanocomposites with controlled morphology and porous structures for environmental applications. In the present work, we have synthesized three-dimensional macroporous rGO–Fe_3O_4 nanocomposites (3D macroporous rGO–Fe_3O_4 nanocomposites) through electrostatic assembly of negatively charged carboxylic graphene oxide (GO-COOH) and cationic poly(methyl methacrylate) (PMMA) microspheres, followed by strong electrostatic interactions with positive Fe^{2+} ions and removal of PMMA template through high temperature calcination treatment. Furthermore, the adsorption properties of 3D macroporous rGO–Fe_3O_4 nanocomposites toward Cr(VI) in aqueous solution have also been investigated.

2 Experimental

2.1 Materials

Carboxylic graphene oxide (GO-COOH) dispersion was purchased from Nanjing XFNANO Materials Tech Co., Ltd. China. Other chemicals of analytical grade were obtained from Sinopharm Chemical Reagent Co. Ltd. China. Ultrapure water was used throughout the experiment.

2.2 Preparation of 3D macroporous rGO–Fe_3O_4 nanocomposites

Poly(methyl methacrylate) (PMMA) microspheres were synthesized through surfactant-free emulsion polymerization using a cationic free radical initiator, as described in a previous report [40]. The obtained PMMA microspheres were positively charged in aqueous solutions and the concentration of PMMA colloidal solution used here was 1.0 wt%. 3D macroporous rGO–Fe_3O_4 nanocomposites were fabricated through electrostatic assembly and high temperature calcination process. 50 ml of GO-COOH dispersion (1 mg/ml) was added dropwise into PMMA colloidal solution (50 ml, 1.0 wt%) under vigorous stirring. After magnetic stirring for 2 h, 30 ml of $FeSO_4 \cdot 7H_2O$ aqueous solution (0.1 mol/l) was added dropwise into the mixture followed by magnetic stirring for 10 h. The resulting product was collected, dried and transferred into tube furnace and calcined at 600 °C for 3 h under nitrogen atmosphere.

2.3 Cr(VI) adsorption experiment

Analytical-grade potassium dichromate ($K_2Cr_2O_7$) was used to prepare Cr(VI) stock solution. Briefly, the Cr(VI) solutions were mixed with predetermined amount of as-prepared 3D macroporous rGO–Fe_3O_4 nanocomposites. The mixed solutions were stirred on a shaking incubator with a shaking speed of 200 rpm at room temperature for a certain time. Then 3D macroporous rGO–Fe_3O_4 nanocomposite adsorbents were separated from the solutions by an external magnetic field. Removal efficiency of Cr(VI) was calculated by measuring the Cr(VI) concentration before and after adsorption. The Cr(VI) concentrations were determined by an inductively coupled plasma-atomic emission spectrometer (ICP-AES). Desired pH values of Cr(VI) solution were adjusted by adding hydrochloric acid or sodium hydroxide solutions.

The adsorption capacity was calculated according to the following equation:

$$q = \frac{(C_0 - C_e)V}{m} \tag{1}$$

where q (mg/g) is the amount adsorbed per unit mass, C_0 (mol/L) is the initial Cr(VI) concentration in solution, C_e (mol/L) is the equilibrium concentration after adsorption, V (L) is the solution volume, and m (g) is the mass of the adsorbent used.

2.4 Desorption and regeneration experiment

For desorption and regeneration, 3D macroporous rGO–Fe_3O_4 nanocomposite adsorbent was subjected to successive adsorption–desorption cycle experiments. After the adsorbent was magnetically separated from the solution and washed well. Desorption of Cr(VI)-laden 3D macroporous rGO–Fe_3O_4 adsorbent was tested using NaOH (0.01, 0.05, 0.1, 0.2, 0.3 mol/l) solution. At the end of each adsorption–desorption cycle, the adsorbent was washed several times with deionized water to remove excess base from the adsorbent surface. The reusability of 3D macroporous rGO–Fe_3O_4 nanocomposite adsorbent for Cr(VI) adsorption was evaluated by conducting five consecutive adsorption–desorption cycles.

2.5 Characterization

X-ray diffraction (XRD) patterns were collected on a Rigaku SmartLab X-ray diffractometer (40 kV, 30 mA). Fourier transform infrared spectrophotometry (FTIR) spectra were recorded using a Varian Cary 670 FTIR spectrometer. Raman spectra were obtained with a Renishaw inVia Raman spectrometer, using a He-Ne laser with an excitation wavelength of 532 nm. Scanning electron microscopy (SEM) measurements were conducted with a Hitachi S-3400N electron microscope operated at 20 kV. Transmission electron microscopy (TEM) and high-resolution transmission electron microscopy (HRTEM) observations were carried out on a JEOL 2011 transmission electron microscopy with an accelerating voltage of 200 kV. Nitrogen adsorption–desorption was determined using a Tristar-3020 surface area analyzer and samples were outgassed at 200 °C under vacuum for 12 h before analysis. The specifc surface area was calculated using Brunauer–Emmett–Teller (BET) method. Magnetic properties were measured using a VSM 7400 vibrating sample magnetometer (VSM) (Lake Shore) with a maximum applied continuous field of 18,000 G at room temperature.

3 Results and discussion

The formation mechanism of 3D macroporous rGO–Fe_3O_4 nanocomposites is illustrated in Fig. 1. The procedure can be divided into three stages. In the first stage, negatively charged GO-COO^- sheets are coated onto the surface of positively charged PMMA microspheres through electrostactic self-assembly. In the second stage, the positive Fe^{2+} ions are loaded onto negative GO-COO^- sheets by strong electrostatic interactions, thus forming $PMMA^+$/GO-COO^-/Fe^{2+} comoposite microspheres. The large specific surface area and expanded interlayer distance of negative GO sheets are highly beneficial for effective anchoring of positive Fe^{2+} ions. Finally, 3D macroporous rGO–Fe_3O_4 nanocomposites are produced by thermal annealing of the above $PMMA^+$/GO-COO^-/Fe^{2+} comoposite microspheres in nitrogen atmosphere. After high temperature calcination, the PMMA template is pyrolyzed and liberated as gaseous products from the composites. Therefore, the $PMMA^+$/GO-COO^-/Fe^{2+} comoposite microspheres are successfully converted into 3D macroporous rGO–Fe_3O_4 nanocomposites.

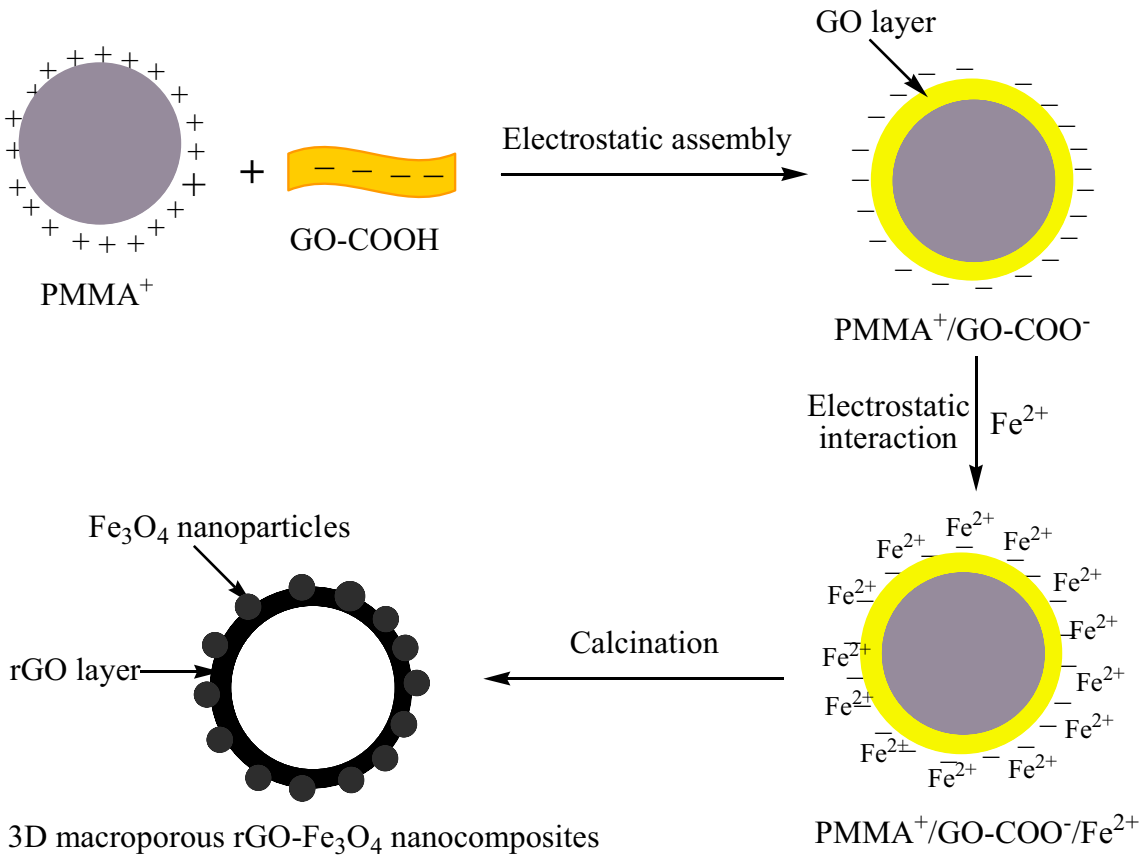

Fig. 1 Schematic illustration of formation mechanism of 3D macroporous rGO–Fe_3O_4 nanocomposites

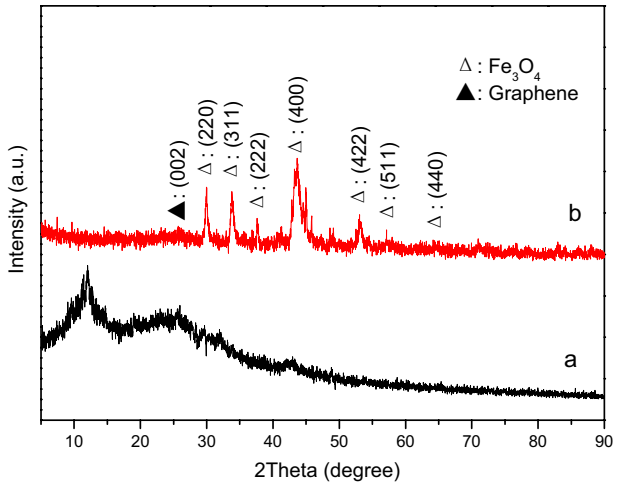

Fig. 2 XRD pattern of (**a**) GO-COOH and (**b**) 3D macroporous rGO–Fe_3O_4 nanocomposites

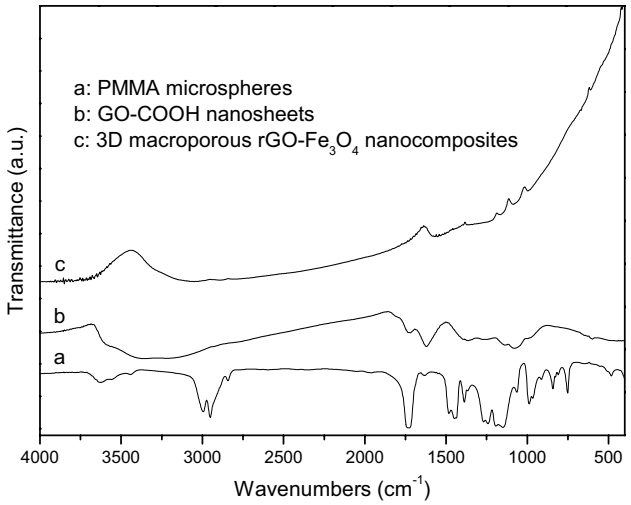

Fig. 3 FT-IR spectra of (**a**) PMMA microspheres, (**b**) GO-COOH nanosheets and (**c**) 3D macroporous rGO–Fe_3O_4 nanocomposites

Wide-angle X-ray diffraction measurement was carried out to investigate the phase structure of samples. The XRD pattern of GO-COOH shows three peaks (Fig. 2a), including a very strong peak 2θ = 11.9° and two weak peaks at 2θ = 25.7° and 42.9°. The major peak at 11.9° corresponds to (002) inter layer spacing of GO and indicates the incorporation of oxygen containing functional groups between the layered GO structure. The peaks at 2θ = 25.7° and 42.9° indicate that the original lamellar structure of graphite has been delaminated into disordered flakes of GO-COOH to some extent [41, 42]. XRD pattern of 3D macroporous rGO–Fe_3O_4 nanocomposites is shown in Fig. 2b. The diffraction peaks match well with standard XRD patterns of Fe_3O_4 and graphene. The diffraction peaks at 2θ values of 30.2°, 34.0°, 37.7°, 43.6°, 53.2°, 57.7° and 64.5° correspond to (220), (311), (222), (400), (422), (511) and (440) facets of face centered cubic structure of Fe_3O_4, respectively [43, 44], suggesting the existence of Fe_3O_4 in the nanocomposites. The weak and broad diffraction peak at 25.6° is corresponding to the (002) reflection of rGO [45]. The characteristic peak of GO-COOH located at 11.9° has disappeared, confirming successful reduction of GO to rGO after high temperature calcinations process [46].

The chemical bonding structure of samples was demonstrated by FT-IR spectroscopy analysis. As seen in Fig. 3a, FT-IR spectrum of PMMA microspheres indicates the presence of C-H stretching vibration of CH_2 and CH_3 group (2800–3000 cm^{-1}), C-H bending vibration (1388, 1484cm^{-1}), C=O stretching vibration (1730 cm^{-1}), and C–O–C stretching vibration (1150, 1194, 1243, 1271cm^{-1}) [47]. After high temperature heat treatment, no characteristic bands of PMMA are found, indicating the complete decomposition of PMMA template. FT-IR spectrum of GO-COOH (Fig. 3b) indicates the presence of oxygen-containing functional groups [48]. The broad bands at about 3400 cm^{-1} are attributed to the stretching of O-H. The peak at 1727.7 cm^{-1} corresponds to the stretching band of C=O in carboxylic acid or carbonyl moieties. The peak at 1624.1 cm^{-1} (aromatic C=C) indicates the presence of sp^2 hybridized honeycomb lattice [49]. In comparison with the spectrum of GO-COOH, no stretching vibration of carboxyl groups are observed in that of 3D macroporous rGO–Fe_3O_4 nanocomposites (Fig. 3c), indicating that the bulk of oxygen-containing functional groups have been removed after calcination. Furthermore, in the FT-IR spectrum of 3D macroporous rGO–Fe_3O_4 nanocomposites, the absorption band at 1578.8 cm^{-1} can be attributed to the skeletal vibration of graphene materials, demonstrating that GO-COOH has been reduced into graphene [50]. The peak appearing at 610.4 cm^{-1} is corresponding to the stretching vibration of Fe–O in Fe_3O_4 [51, 52].

Raman spectroscopy is a powerful, nondestructive tool to characterize carbonaceous materials. Raman spectra of GO-COOH and 3D macroporous rGO–Fe_3O_4 nanocomposites are shown in Fig. 4. Two prominent peaks corresponding to G and D bands are observed clearly. It is known that the D band originates from a breathing k-point phonon with A_{1g} symmetry and relates to local structural defects and disorders, or edges of graphene. The G band corresponds to the first-order scattering of E_{2g} mode for sp^2 carbon domains [53]. The intensity ratio of D and G band (I_D/I_G) is used to evaluate the disordered crystal structures of carbon materials [54]. The ratio of intensities (I_D/I_G) for 3D macroporous rGO–Fe_3O_4 nanocomposites is 0.91, which is larger than that of GO-COOH (0.86), indicating the presence of localized sp^3 defects within the sp^2 carbon network after reduction of GO-COOH and increased disordered degree resulting from

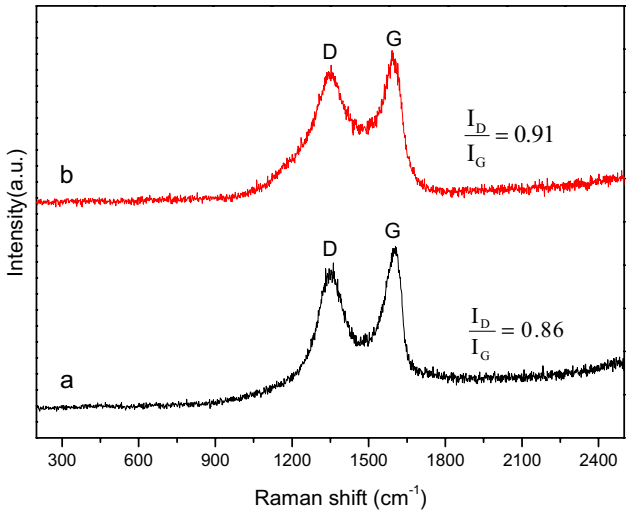

Fig. 4 Raman spectra of **a** GO-COOH and **b** 3D macroporous rGO–Fe_3O_4 nanocomposites

the deposition of Fe_3O_4 nanoparticles onto the surface of rGO [55, 56].

Scanning electron microscopy was utilized to investigate the morphology and structure of samples. The PMMA particles show a spherical and mono-dispersed structure with an average diameter of 250 nm (Fig. 5a). The crumpled and wrinkled GO sheets are uniformly coated onto PMMA microspheres without much undulation (Fig. 5b), revealing the strong electrostatic interactions between cationic PMMA particles and negative GO sheets. Compared with $PMMA^+$/GO-COO^- microspheres, $PMMA^+$/GO-COO^-/Fe^{2+} hybrids have more attachments (Fig. 5c), presenting slight deformation on the surface, indicating a stronger electrostatic attraction force between negatively charged GO nanosheets and positive Fe^{2+} species. The electrostatic attraction force plays an important role in controlling the surface morphology and core–shell structure of composite microspheres. The as-prepared rGO–Fe_3O_4 nanocomposite exhibits a well-defined 3D macroporous architecture with a pore size of about 200–250 nm (Fig. 5d). The spherical macropores composed of graphene nanosheets can be clearly observed,

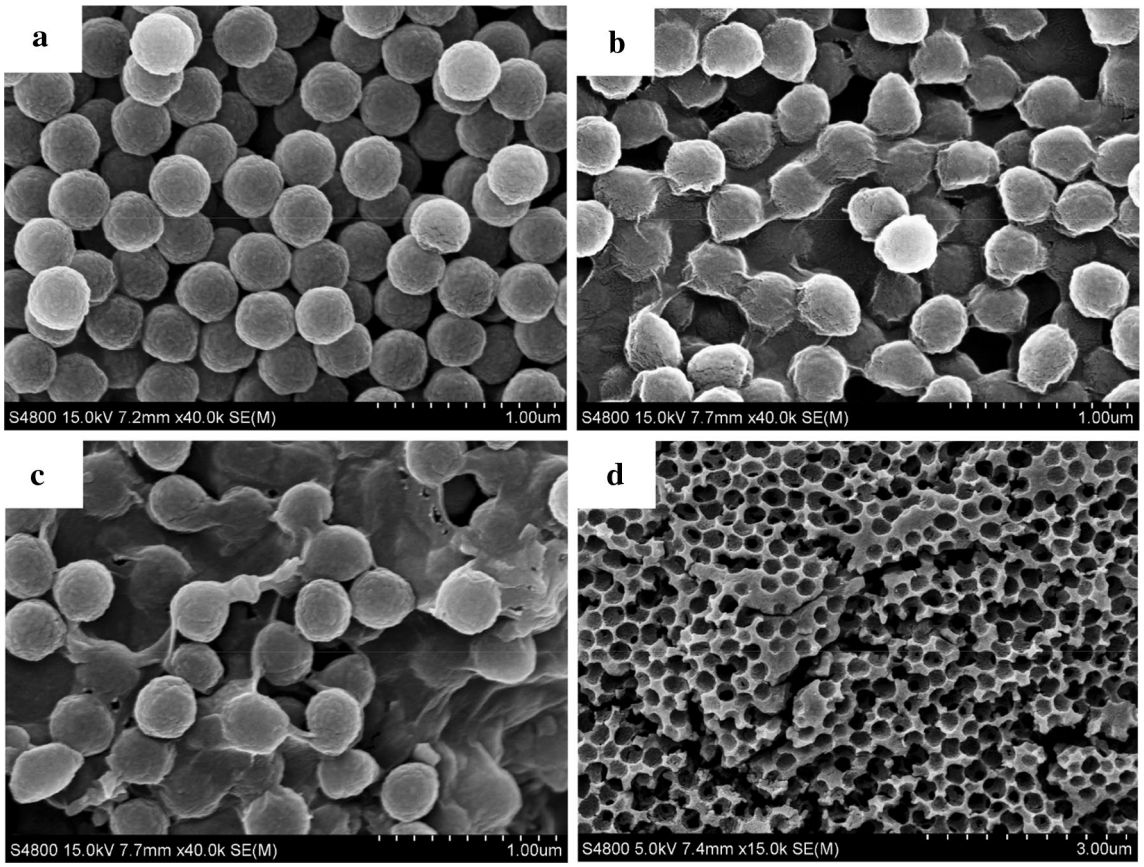

Fig. 5 SEM images of **a** PMMA microsperes, **b**$PMMA^+$/GO-COO^- microspheres, **c** $PMMA^+$/GO-COO^-/Fe^{2+} hybrids, **d** 3D macroporous rGO–Fe_3O_4 nanocomposites

indicating the spherical PMMA templates have been removed completely.

The morphology and structure of samples were further investigated by transmission electron microscopy. It can be seen that Fe_3O_4 nanoparticles are uniformly decorated and firmly anchored on the graphene framework (Fig. 6a). The average size of Fe_3O_4 nanoparticles is 4.9 nm. The distinctive lattice structure unambiguously confirms that high-quality graphene sheets maintain their structural integrity without obvious defects after deposition Fe_3O_4 nanoparticles. Notably, the graphene nanosheets may favor to hinder Fe_3O_4 nanoparticles from agglomeration and enable their good distribution on the graphene surface, while Fe_3O_4 nanoparticles serve as stabilizer for separating graphene nanosheets from aggregation. A representative HRTEM image of 3D macroporous rGO–Fe_3O_4 nanocomposite is shown in Fig. 6b. It can be seen that Fe_3O_4 nanoparticles are well crystallized and the lattice spacing between two adjacent crystal planes is 0.25 nm, which agrees well with (311) planes of Fe_3O_4 crystals [57]. These results reveal the successful decoration of Fe_3O_4 nanoparticles onto the surface of rGO.

The nitrogen adsorption–desorption isotherms and corresponding pore size distribution curves of 3D macroporous rGO–4Fe_3O_4 nanocomposites are shown in Fig. 7. The sharply increased nitrogen uptake at lower relative pressure region ($P/P_0 < 0.01$) demonstrates the existence of abundant micropores. The isotherms show typical type IV and type H_3 hysteresis loop (Fig. 7a), indicating a clear capillary condensation derived from mesopores. The specific surface area, total pore volume and micropore volume are 533 m^2/g, 0.51 and 0.17 cm^3/g, respectively. Such values are comparable to some reported works [58–60]. The higher specific surface

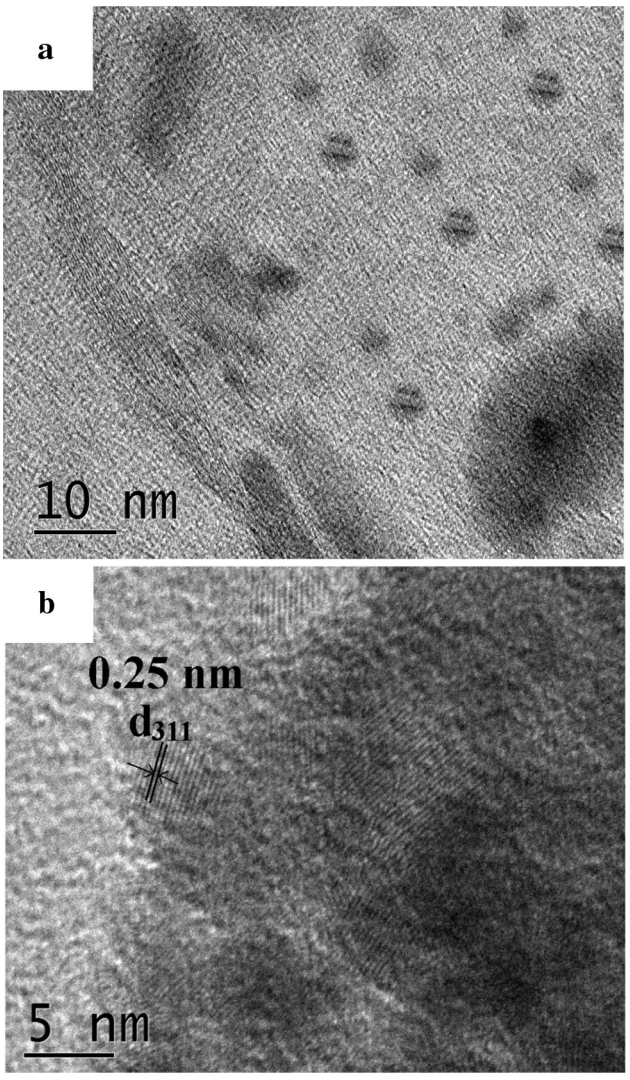

Fig. 6 TEM (**a**) and HRTEM (**b**) images of 3D macroporous rGO–Fe_3O_4 nanocomposites

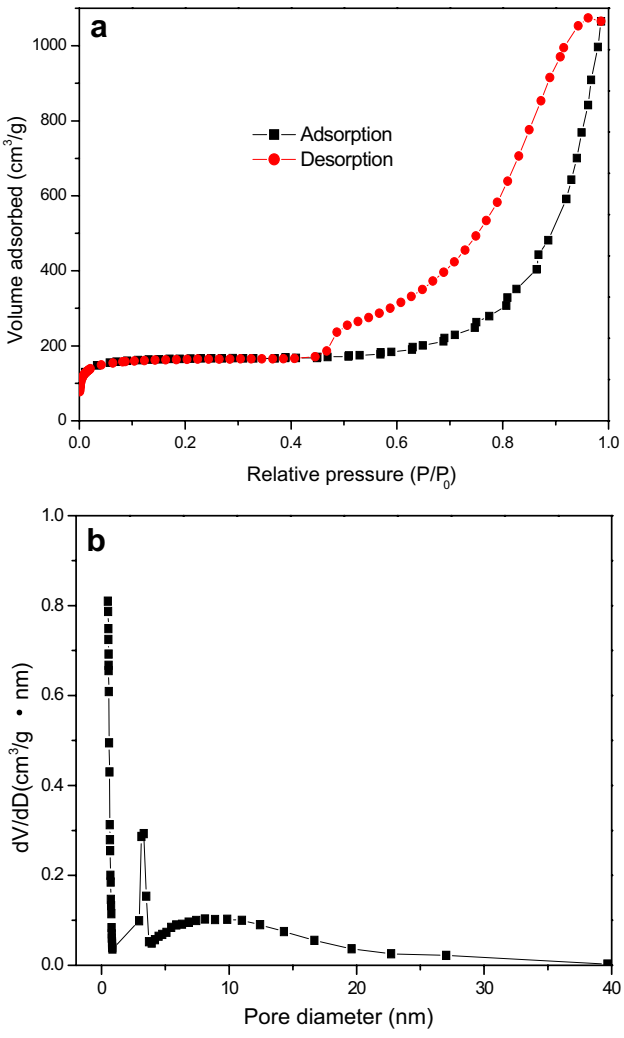

Fig. 7 Nitrogen adsorption–desorption isotherms (a) and corresponding pore size distribution (b) of 3D macroporous rGO–Fe_3O_4 nanocomposites

area and big pore volume can be attributed to the formed secondary pores after removal of PMMA templates. The pore size distribution curve exhibits typical bimodal mesopores with pore size of 3.3 and 9.5 nm (Fig. 7b). Therefore, combined with SEM and TEM measurements, as-prepared 3D macroporous rGO–Fe_3O_4 nanocomposite has a hierarchical porous structure with multi-level pores (macro-, meso-, and micropores), which have increased adsorption performance compared with single-sized porous carbon materials due to the structural advantages from pores of different size ranges. The macropores can provide interconnected framework and mass transport channels, while meso-/micro-pores are beneficial for generating high specific surface areas [61].

The magnetization measurement for the as-prepared 3D macroporous rGO–Fe_3O_4 nanocomposite was carried out using vibrating sample magnetometer at room temperature, as shown in Fig. 8. The magnetization hysteresis loop is S-like curve, indicating that 3D macroporous rGO–Fe_3O_4 nanocomposite is superparamagnetic. The measured saturation magnetization (M_s) of 3D macroporous rGO–Fe_3O_4 nanocomposite is 22.66 emu/g, which is lower than that of pure Fe_3O_4 nanocrystals due to the presence of graphene [62]. However, this magnetization is strong enough for fast magnetic separation during the adsorption experiments.

Figure 9 shows the influence of initial solution pH value on the removal of Cr(VI) by 3D macroporous rGO–Fe_3O_4 nanocomposites. It can be seen that the removal capacity decreases dramatically as the initial solution pH value increases. At lower pH value, the most prevalent species of Cr(VI) is $HCrO_4^-$, but as the pH value increases, this form shifts to $Cr_2O_7^{2-}$. At lower pH value, the adsorbent becomes highly protonated and positively charged, which favors the uptake of Cr(VI) anions through electrostatic attraction. Higher pH value will decline the extent of protonation and

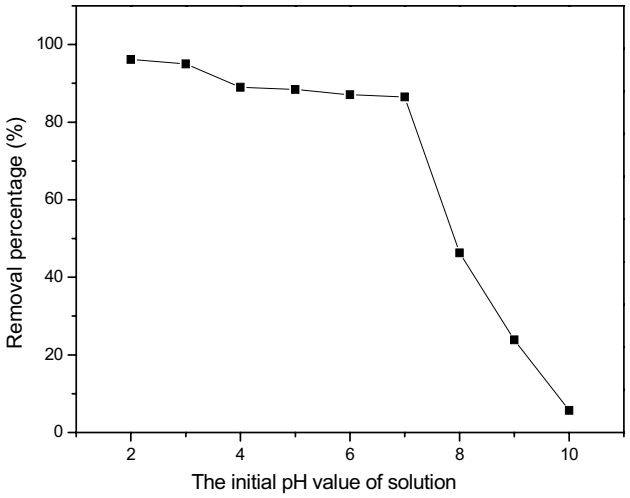

Fig. 9 Effects of pH value on the Cr(VI) removal efficiency of 3D macroporous rGO–Fe_3O_4 nanocomposite adsorbent

weaken the electrostatic attraction between the sorbent and negatively charged Cr(VI) anions, thus decreasing the uptake of Cr(VI) [63]. Although the adsorption capacity decreases with the increase of pH value, it still remains significant adsorption ability in the examined pH range.

Figure 10 displays the variation of adsorption capacity of 3D macroporous rGO–Fe_3O_4 nanocomposite for Cr(VI) with the contact time at pH 2. It can be seen that a fast adsorption process of Cr(VI) occurs during the first few minutes. The adsorbed amount of Cr(VI) reaches its equilibrium value in about 30 min. To further investigate the adsorption behavior of Cr(VI) onto 3D macroporous rGO–Fe_3O_4 nanocomposite adsorbent, the kinetic data are evaluated by

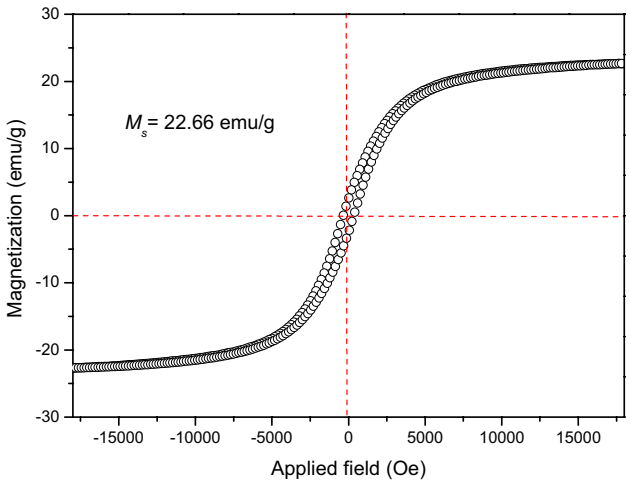

Fig. 8 Magnetization hysteresis loop of 3D macroporous rGO–Fe_3O_4 nanocomposites

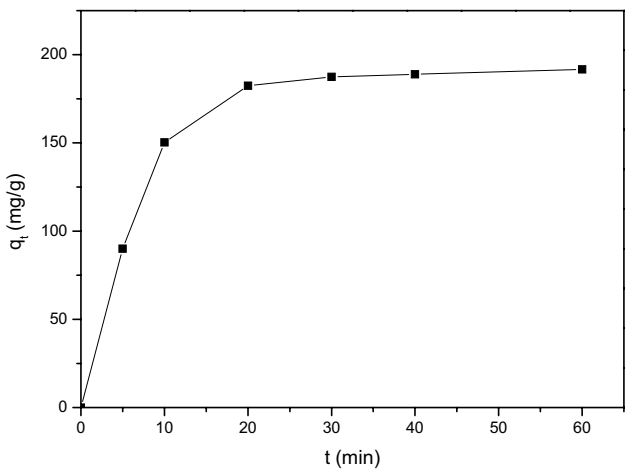

Fig. 10 Adsorption capacity of Cr(VI) onto 3D macroporous rGO–Fe_3O_4 nanocomposite adsorbent at room temperature (pH 2)

pseudo-first-order equation and pseudo-second-order equation, which are described by the following equations.

$$\log(q_e - q_t) = \log q_e - \frac{k_1 t}{2.303} \quad (2)$$

$$\frac{t}{q_t} = \frac{1}{k_2 q^2_e} + \frac{t}{q_e} \quad (3)$$

where k_1 (min^{-1}) and k_2 (g/mg min) are the rate constant for pseudo-first-order and pseudo-second-order adsorption kinetics, respectively. q_e and q_t are the amounts of Cr(VI) adsorbed (mg/g) at equilibrium and time t (min), respectively. Figure 11a indicates the linear dependence between $\log(q_e - q_t)$ and t, where the values of k_1 and q_e can be obtained from the intercept and slope of the plot. Meanwhile, k_2 and q_e can be determined by the intercept and slope of the linear plot t/q_t versus t in Fig. 11b. The corresponding kinetics parameters and correlation coefficients are listed in Table 1. It can be seen that the correlation coefficient R^2 calculated by pseudo-first-order is smaller than that of pseudo-second-order model. It means that the pseudo-second-order model is more suitable to describe the adsorption kinetics of 3D macroporous rGO–Fe_3O_4 nanocomposite adsorbent for Cr(VI).

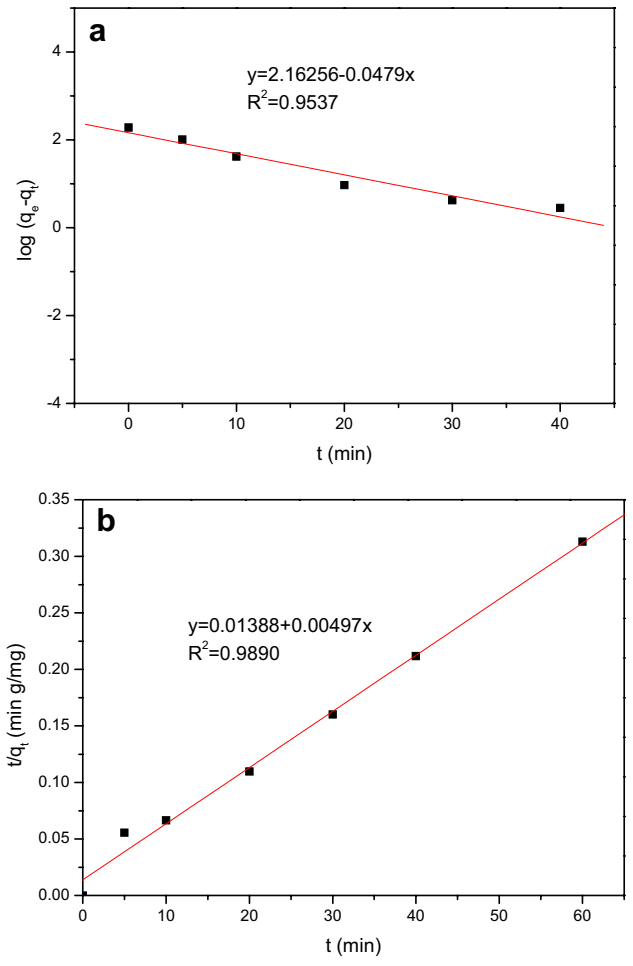

Fig. 11 Adsorption kinetic for Cr(VI) adsorption onto 3D macroporous rGO–Fe_3O_4 nanocomposite adsorbent. a Pseudo-first-order model and b pseudo-second-order model

Table 1 Kinetics parameters for adsorption of Cr(VI) onto 3D macroporous rGO–Fe_3O_4 nanocomposite

Kinetic model	Parameters			
Pseudo-first-order	$q_{e,exp}$ (mg/g)	k_1 (min^{-1})	$q_{e,cal}$ (mg/g)	R^2
	191.7	0.1103	145.4	0.954
Pseudo-second-order	$q_{e,exp}$ (mg/g)	k_2 (min^{-1})	$q_{e,cal}$ (mg/g)	R^2
	191.7	0.0018	201.2	0.989

The equilibrium adsorption isotherm is very important to analyze the surface properties of adsorbents. The classical Langmuir model and Freundlich model are used to evaluate the adsorption performance of 3D macroporous rGO–Fe_3O_4 nanocomposite adsorbent. The Langmuir isotherm assumes a homogeneous adsorption surface of the adsorbent, where all the adsorption sites are identical and energetically equivalent. However, the Freundlich isotherm describes a heterogeneous adsorption system and the adsorption sites are diverse. The Langmuir model and Freundlich model are expressed by the following equations, respectively.

$$\frac{C_e}{q_e} = \frac{C_e}{q_{\max}} + \frac{1}{k_L q_{\max}} \quad (4)$$

$$\log q_e = \log k_F + \frac{1}{n} \log C_e \quad (5)$$

here, C_e (mg/l) and q_e (mg/g) are the concentration and the adsorption capacity of Cr(VI) at equilibrium, $q_{\max}$ (mg/g) is the maximum monolayer adsorption capacity, and k_L (l/mg) is the constant related to the energy of adsorption, which can be determined by the slope and intercept of the linear plot C_e/q_e versus C_e, respectively (in Fig. 12a). Meanwhile, k_F and 1/n are the Freundlich equilibrium constant indicative of adsorption and the Freundlich adsorption constant, which can be calculated from intercept and slope of the linear plot between $\log C_e$ and $\log q_e$, respectively (in Fig. 12b). Based on the above isotherm models, the calculated parameters are listed in Table 2. It can be seen that the adsorption of Cr(VI) on 3D macroporous rGO–Fe_3O_4 nanocomposite adsorbent is better described by the Langmuir isotherm model with higher correlation coefficients (R^2), which means the adsorption of Cr(VI) onto 3D macroporous rGO–Fe_3O_4 nanocomposite adsorbent is a monolayer adsorption.

Evaluation of the reusability of adsorbent is a primary condition to promote an adsorbent as a practical and

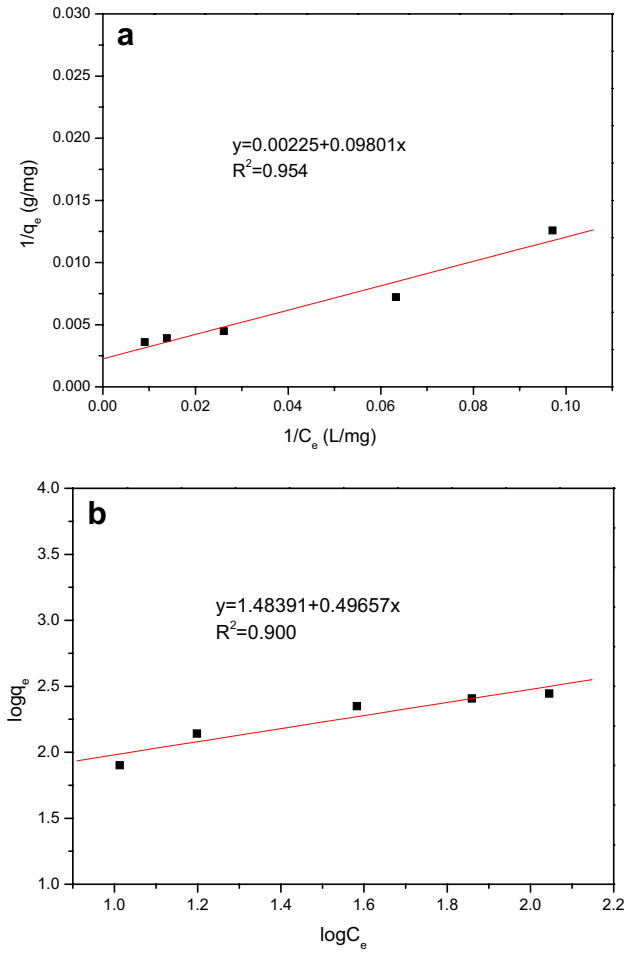

Fig. 12 Adsorption isotherms for Cr(VI) adsorption onto 3D macroporous rGO–Fe_3O_4 nanocomposite adsorbent. (a) Langmuir isotherm and (b) Freundlich isotherm

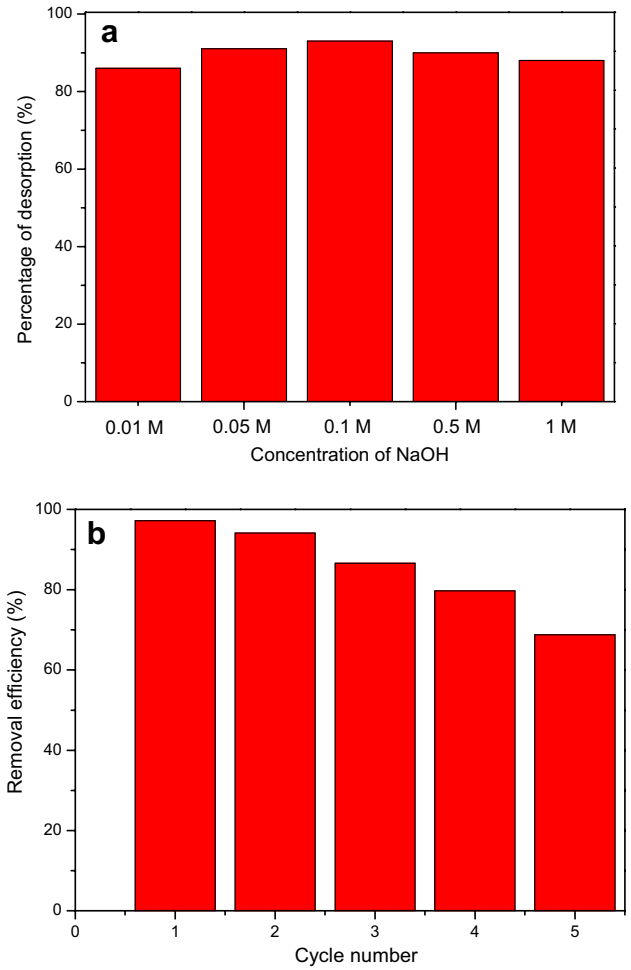

Fig. 13 **a** Desorption of Cr(VI) from 3D macroporous rGO–Fe_3O_4 nanocomposite adsorbent using different concentration of NaOH solution and **b** the reusability of 3D macroporous rGO–Fe_3O_4 nanocomposite adsorbent

Table 2 Isotherm parameters for adsorption of Cr(VI) onto 3D macroporous rGO–Fe_3O_4 nanocomposite

Isotherm model	Parameters		
Langmuir	k_L (L/mg)	q_m (mg/g)	R^2
	0.0232	448.0	0.954
Freundlich	k_F (mg/g)	n	R^2
	30.47	2.01	0.900

economical one. Different concentration of NaOH solution is used to desorb Cr(VI) from 3D macroporous rGO–Fe_3O_4 nanocomposite adsorbent. It can be seen from Fig. 13a that 0.1 M NaOH is the optimum concentration for the effective desorption. The Cr(VI) removal percentage by 3D macroporous rGO–Fe_3O_4 nanocomposite adsorbent for five consecutive adsorption–desorption cycles is presented in Fig. 13b. It is observed that the Cr(VI) removal efficiency decreases slightly after each subsequent cycle. After first and five runs, the removal efficiency decreases to 97.2 and 68.8%, respectively, suggesting the excellent reusability of 3D macroporous rGO–Fe_3O_4 nanocomposite adsorbents.

4 Conclusion

In summary, three-dimensional macroporous reduced graphene oxide–Fe_3O_4 nanocomposites have been successfully fabricated through electrostatic self-assembly of negatively charged GO-COOH and cationic PMMA microspheres, followed by strong electrostatic interactions with positive Fe^{2+} ions and then high temperature calcination treatment to remove PMMA template. The obtained 3D macroporous rGO–Fe_3O_4 nanocomposite has a hierarchical porous structure with multi-level pores (macro-, meso-, and micropores), and exhibits high specific surface area and large pore

volume. These advantages guarantee the excellent adsorption performance of 3D macroporous rGO–Fe_3O_4 nanocomposites, which have high adsorption capacities, rapid adsorption rates and convenient magnetic separation for reusability. The kinetics of adsorption follows the pseudo-second-order mechanism. The results from equilibrium models indicate that Langmuir model can be better used to describe the experimental data. The study will provide a basis for designing three-dimensional graphene-based nanocomposites with controlled morphology and porous structures for practical environmental applications.

Acknowledgements The authors gratefully acknowledge the financial supports from Basic and Frontier Research Program of Chongqing Municipality (cstc2016jcyjA0140) and Innovation Team Project of Chongqing Municipal Education Commission (CXTDX201601037).

References

1. A. Zhitkovich, Chem. Res. Toxicol. **24**, 1617–1629 (2011)
2. Z.W. Xu, Y.Y. Zhang, X.M. Qian, J. Shi, L. Chen, B.D. Li, J.R. Niu, L.S. Liu, Appl. Surf. Sci. **316**, 308–314 (2014)
3. P. Tan, J. Sun, Y.Y. Hu, Z. Fang, Q. Bi, Y.C. Chen, J.H. Cheng, J. Hazard. Mater. **297**, 251–260 (2015)
4. M. Pirveysian, M. Ghiaci, Appl. Surf. Sci. **428**, 98–109 (2018)
5. Z.M. Wang, X.J. Li, H.J. Liang, J.L. Ning, Z.D. Zhou, G.Y. Li, Mater. Sci. Eng. C **79**, 227–236 (2017)
6. M.A. Behnajady, S. Bimeghdar, Chem. Eng. J. **239**, 105–113 (2014)
7. R. Chen, L. Chai, Q. Li, Y. Shi, Y. Wang, A. Mohammad, Environ. Sci. Pollut. Res. Int. **20**, 7175–7185 (2013)
8. X. Wang, Y.H. Liang, W.J. An, J.S. Hu, Y.F. Zhu, W.Q. Cui, Appl. Catal. B: Environ. **219**, 53–62 (2017)
9. M.O. Ansari, R. Kumar, S.A. Ansari, S.P. Ansari, M.A. Barakat, A. Alshahrie, M.H. Cho, J. Colloid Interf. Sci. **496**, 407–415 (2017)
10. S. Velazquez-Peña, C. Barrera-Díaz, I. Linares-Hernández, B. Bilyeu, S.A. Martínez-Delgadillo, Ind. Eng. Chem. Res. **51**, 5905–5910 (2012)
11. R.W. Liang, L.J. Shen, F.F. Jing, N. Qin, L. Wu, ACS Appl. Mater. Interfaces **7**, 9507–9515 (2015)
12. F.S. Awad, K.M. AbouZeid, W.M. Abou El-Maaty, A.M. El-Wakil, M. Samy El-Shall, ACS Appl. Mater. Interfaces **9**, 34230–34242 (2017)
13. T.T. Luo, X.K. Tian, C. Yang, W.J. Luo, Y.L. Nie, Y.X. Wang, J. Agric. Food Chem. **65**, 7153–7158 (2017)
14. Y.Q. Xing, X.M. Chen, D.H. Wang, Environ. Sci. Technol. **41**, 1439–1443 (2017)
15. S. Mishra, A. Yadav, N. Verma, Chem. Eng. J. **326**, 987–999 (2017)
16. S.W. Yang, X.P. Huang, G. Chen, E.N. Wang, J. Porous Mat. **23**, 1647–1652 (2016)
17. S. Chae, S. Jang, W.J. Choi, Y.S. Kim, H. Chang, T.I. Lee, J.O. Lee, Nano Lett. **17**, 1711–1718 (2017)
18. K.S. Ranjith, P. Manivel, R.T. Rajendrakumar, T. Uyar, Chem. Eng. J. **325**, 588–600 (2017)
19. B. Szczęśniak, Ł Osuchowski, J. Choma, M. Jaroniec, J. Porous Mat. **25**, 621–627 (2018)
20. X.J. Tao, X.D. Wang, Z.W. Li, S.M. Zhou, Appl. Surf. Sci. **324**, 363–368 (2015)
21. W.F. Zhao, Y.S. Tang, J. Xi, J. Kong, Appl. Surf. Sci. **326**, 276–284 (2015)
22. W.J. Peng, H.Q. Li, Y.Y. Liu, S.X. Song, J. Mol. Liq. **230**, 496–504 (2017)
23. J. Wang, B.L. Chen, Chem. Eng. J. **281**, 379–388 (2015)
24. Y. Wu, F. Yang, X.X. Liu, G.Q. Tan, D. Xiao, Appl. Surf. Sci. **435**, 281–289 (2018)
25. J. Xu, Z. Cao, Y.L. Zhang, Z.L. Yuan, Z.M. Lou, X.H. Xu, X.K. Wang, Chemosphere **195**, 351–364 (2018)
26. W.C. Cheng, C.C. Ding, X.Q. Nie, T. Duan, R.R. Ding, ACS Sustainable Chem. Eng. **5**, 5503–5511 (2017)
27. D. Vilela, J. Parmar, Y.F. Zeng, Y.L. Zhao, S. Sánchez, Nano Lett. **16**, 2860–2866 (2016)
28. L.L. Liu, L. Ding, X. Wu, F. Deng, R.F. Kang, X.B. Luo, Ind. Eng. Chem. Res. **55**, 6845–6853 (2016)
29. L.P. Pan, S.L. Liu, O. Oderinde, K.W. Li, F. Yao, G.D. Fu, Appl. Surf. Sci. **427**, 779–786 (2018)
30. F. Wang, X.W. Lu, W.C. Peng, Y. Deng, T. Zhang, Y.B. Hu, X.Y. Li, ACS Omega **2**, 5378–5384 (2017)
31. S.B. Ye, Y. Liu, J.C. Feng, ACS Appl. Mater. Interfaces **9**, 22456–22464 (2017)
32. J.P. Zou, H.L. Liu, J.M. Luo, Q.J. Xing, H.M. Du, X.H. Jiang, X.B. Luo, S.L. Luo, S.L. Sui, ACS Appl. Mater. Interfaces **8**, 18140–18149 (2016)
33. B. Tan, H.M. Zhao, Y.B. Zhang, X. Quan, Z.H. He, W.T. Zheng, B.Y. Shi, J. Colloid Interf. Sci. **512**, 853–861 (2018)
34. Z.J. Li, Z.W. Huang, W.L. Guo, L. Wang, L.R. Zheng, Z.F. Chai, W.Q. Shi, Environ. Sci. Technol. **51**, 5666–5674 (2017)
35. R. Guo, T.F. Jiao, R.F. Li, Y. Chen, W.C. Guo, L.X. Zhang, J.X. Zhou, Q.R. Zhang, Q.M. Peng, ACS Sustainable Chem. Eng. **6**, 1279–1288 (2018)
36. X. Li, S.F. Wang, Y.G. Liu, L.H. Jiang, B. Song, M.F. Li, G.M. Zeng, X.F. Tan, X.X. Cai, Y. Ding, J. Chem. Eng. Data **62**, 407–416 (2017)
37. K. Luo, Y.Y. Mu, P. Wang, X.T. Liu, Appl. Surf. Sci. **359**, 188–195 (2015)
38. N. Li, H.L. Jiang, X.L. Wang, X. Wang, G.J. Xu, B.B. Zhang, L.J. Wang, R.S. Zhao, J.M. Lin, TrAC Trend. Anal. Chem. **102**, 60–74 (2018)
39. W. Wang, K. Cai, X.F. Wu, X.H. Shao, X.J. Yang, J. Alloy. Compd. **722**, 532–543 (2017)
40. V.H. Pham, T.T. Dang, S.H. Hur, E.J. Kim, J.S. Chung, ACS Appl. Mater. Interfaces **4**, 2630–2636 (2012)
41. H.W. Yang, M.Y. Hua, S.L. Chen, R.Y. Tsai, Biosens. Bioelectron. **41**, 172–179 (2013)
42. W.K. Park, J.H. Jung, J. Power Sources **199**, 379–385 (2012)
43. I.F. Nata, G.W. Salim, C.-K. Lee, J. Hazard. Mater. **183**, 853–858 (2010)
44. G.X. Wang, J. Yang, J. Park, X.L. Gou, B. Wang, H. Liu, J. Yao, J. Phys. Chem. C **112**, 8192–8195 (2008)
45. Y. Zhu, M.I.D. Stoller, W. Cai, A. Velamakanni, R.D. Piner, D. Chen, R.S. Ruoff, ACS Nano **4**, 1227–1233 (2010)
46. C. Zhu, S. Guo, Y. Fang, S. Dong, ACS Nano **4**, 2429–2437 (2010)
47. K. Moller, T. Bein, R.X. Fischer, Chem. Mater. **10**, 1841–1852 (1998)
48. G. Xie, P. Xi, H. Liu, F. Chen, L. Huang, Y. Shi, F. Hou, Z. Zeng, C. Shao, J. Wang, J. Mater. Chem. **22**, 1033–1039 (2012)
49. T.N. Narayanan, Z. Liu, P.R. Lakshmy, W. Gao, Y. Nagaoka, D.S. Kumar, J. Lou, R. Vajtai, P.M. Ajayan, Carbon **50**, 1338–1345 (2012)
50. S.M. Tan, A. Ambrosi, C.K. Chua, M. Pumera, J. Mater. Chem. A **2**, 10668–10675 (2014)
51. L.H. Ai, C.Y. Zhang, Z.L. Chen, J. Hazard. Mater. **192**, 1515–1524 (2011)

52. M.B. Avinash, K.S. Subrahmanyam, Y. Sundarayya, T. Govindaraju, Nanoscale **2**, 1762–1766 (2010)
53. S. Chen, J.W. Zhu, X. Wang, J. Phys. Chem. C **114**, 11829–11834 (2010)
54. J.S. Zhou, H.H. Song, L.L. Ma, X.H. Chen, RSC Adv. **1**, 782–791 (2011)
55. S. Eigler, C. Dotzer, A. Hirsch, Carbon **50**, 3666–3673 (2012)
56. L.G. Cançado, A. Jorio, E.M. Ferreira, F. Stavale, C. Achete, R. Capaz, M. Moutinho, A. Lombardo, T. Kulmala, A. Ferrari, Nano Lett. **11**, 3190–3196 (2011)
57. G.M. Zhou, D.W. Wang, F. Li, L.L. Zhang, N. Li, Z.S. Wu, L. Wen, G.Q. Lu, H.M. Cheng, Chem. Mater. **22**, 5306–5313 (2010)
58. W. Fan, W. Gao, C. Zhang, W.W. Tjiu, J. Pan, T. Liu, J. Mater. Chem. **22**, 25108–25115 (2012)
59. Z. Geng, Y. Lin, X. Yu, Q. Shen, L. Ma, Z. Li, N. Pan, X. Wang, J. Mater. Chem. **22**, 3527–3535 (2012)
60. Y. Yao, S. Miao, S. Liu, L.P. Ma, H. Sun, S. Wang, Chem. Eng. J. **184**, 326–332 (2012)
61. Y.R. Liu, J. Porous Mater. **21**, 1009–1014 (2014)
62. H. Lee, E. Lee, D.K. Kim, N.K. Jang, Y.Y. Jeong, S. Jon, J. Am. Chem. Soc. **128**, 7383–7389 (2006)
63. J.H. Zhu, S.Y. Wei, H.B. Gu, S.B. Rapole, Q. Wang, Z.P. Luo, N. Haldolaarachchige, D.P. Young, Z.H. Guo, Environ. Sci. Technol. **46**, 977–985 (2012)